PHYSICAL REVIEW MATERIALS **7**, 074403 (2023)

Neutron scattering and muon-spin spectroscopy studies of the magnetic triangular-lattice compounds $A_2La_2NiW_2O_{12}$ (A = Sr, Ba)

B. C. Yu,[1,*] J. Y. Yang,[2,3,*] D. J. Gawryluk,[4] Y. Xu,[1] Q. F. Zhan,[1] T. Shiroka,[5,6] and T. Shang[1,7,†]
[1]*Key Laboratory of Polar Materials and Devices (MOE), School of Physics and Electronic Science,*
East China Normal University, Shanghai 200241, China
[2]*Institute of High Energy Physics, Chinese Academy of Sciences (CAS), Beijing 100049, China*
[3]*Spallation Neutron Source Science Center (SNSSC), Dongguan 523803, China*
[4]*Laboratory for Multiscale Materials Experiments, Paul Scherrer Institut, CH-5232 Villigen PSI, Switzerland*
[5]*Laboratory for Muon-Spin Spectroscopy, Paul Scherrer Institut, CH-5232 Villigen PSI, Switzerland*
[6]*Laboratorium für Festkörperphysik, ETH Zürich, CH-8093 Zürich, Switzerland*
[7]*Chongqing Key Laboratory of Precision Optics, Chongqing Institute of East China Normal University, Chongqing 401120, China*

(Received 11 April 2023; revised 24 May 2023; accepted 7 July 2023; published 17 July 2023)

We report on the geometrically frustrated two-dimensional triangular-lattice magnets $A_2La_2NiW_2O_{12}$ ($A = \mathrm{Sr, Ba}$) studied mostly by means of neutron powder diffraction (NPD) and muon-spin rotation and relaxation (μSR) techniques. The chemical pressure induced by the Ba-for-Sr substitution suppresses the ferromagnetic (FM) transition from 6.3 K in the Ba compound to 4.8 K in the Sr compound. We find that the $R\bar{3}$ space group reproduces the NPD patterns better than the previously reported $R\bar{3}m$ space group. Both compounds adopt the same magnetic structure with a propagation vector $\boldsymbol{k} = (0, 0, 0)$, in which the Ni^{2+} magnetic moments are aligned ferromagnetically along the c axis. The zero-field μSR results reveal two distinct internal fields (0.31 and 0.10 T), caused by the long-range FM order. The small transverse muon-spin relaxation rates reflect the homogeneous internal field distribution in the ordered phase and, thus, further support the simple FM arrangement of the Ni^{2+} moments. The small longitudinal muon-spin relaxation rates, in both the ferromagnetic and paramagnetic states of $A_2La_2NiW_2O_{12}$, indicate that spin fluctuations are rather weak. Our results demonstrate that chemical pressure indeed changes the superexchange interactions in $A_2La_2NiW_2O_{12}$ compounds, with the FM interactions being dominant.

DOI: 10.1103/PhysRevMaterials.7.074403

I. INTRODUCTION

Geometric frustration occurs when a system of interacting spins is unable to find its lowest energy state because of how the spins are arranged. This property plays an important role at microscopic scales in solids. In particular, in certain cases, such as in spin glasses, spin ice, and spin liquids [1–4], the localized magnetic moments interact through competing exchange interactions that cannot be simultaneously satisfied, thus giving rise to a highly degenerate magnetic ground state. For instance, in a spin-liquid system, the constituent spins are highly correlated, but still fluctuate strongly down to zero temperature [1,4–8]. Such fluctuations lead to remarkable collective phenomena such as emergent gauge fields and fractional excitations [4,8–10]. Most of the magnetic frustrations have a simple geometric origin [2,11,12], usually occurring in materials with a two-dimensional (2D) triangular or kagome lattice, or a 3D pyrochlore lattice, etc., with the nearest-neighbor interactions being antiferromagnetic (AFM) [13,14].

A two-dimensional triangular lattice with antiferromagnetic interactions provides one of the prototypes of magnetic frustration [13,14]. The perovskite-derived compounds $A_4B'B_2O_{12}$ ($A = \mathrm{Sr, Ba, La}$; $B' = \mathrm{Mn, Co, Ni}$; $B = \mathrm{Sb, Te, W, Re}$) represent one such system [15–18]. Depending on the valence states of the B' and B atoms, the A site can be occupied by either a Sr^{2+} (Ba^{2+}) or La^{3+} ion, or by their combinations. Here, the magnetic B' ions form a layered structure with a threefold site symmetry [see Fig. 1(a) for the $B' = Ni^{2+}$ case]. Since the magnetic B' layers are well separated by nonmagnetic A and BO_6 layers, the former give rise to a magnetic quasi-2D triangular lattice, which can potentially host magnetic frustrations.

To date, different magnetic ground states have been found to occur in the $A_4B'B_2O_{12}$ family [16–18], whose magnetic properties are thought to be determined mostly by the competition between the ferromagnetic (FM) B'-O-B-O-B' and antiferromagnetic B'-O-O-B' superexchange interactions, shown by solid and dashed lines in Fig. 1(c) [16]. The spin state of the magnetic B' ions plays a decisive role in the competition between the two superexchange interactions. As a consequence, $A_4CoB_2O_{12}$ (effective spin $S = 1/2$ for Co^{2+}) and $Ba_2La_2NiW_2O_{12}$ ($S = 1$ for Ni^{2+}) are reported to be ferromagnetic, while $Ba_2La_2MnW_2O_{12}$ ($S = 5/2$ for Mn^{2+}) is reported to be antiferromagnetic [16,19]. Similar superexchange interactions and their competitions have been observed in other triangular-lattice magnets, e.g., $Ba_3B'Nb_2O_9$ [20–23] and $AAg_2B'(VO_4)_2$ [24,25]. Unsurprisingly, such closely competing interactions can be

---

[*] These authors contributed equally to this work.

[†] Corresponding author: tshang@phy.ecnu.edu.cn

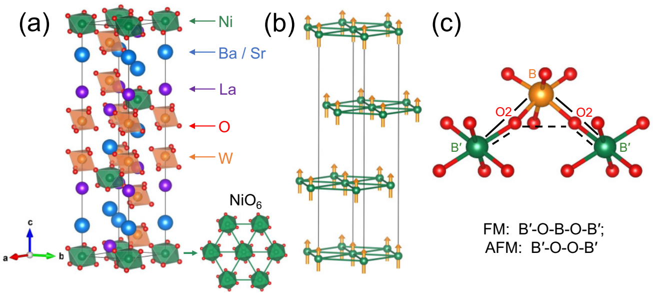

FIG. 1. (a) Crystal structure of $A_2La_2NiW_2O_{12}$ (A = Sr, Ba). The Ni layers form triangular lattices. (b) Sublattice of Ni^{2+} ions showing that the magnetic moments (indicated by arrows) point along the c axis. (c) Pathways of the FM B'-O-B-O-B' (black solid line) and AFM B'-O-O-B' (black dashed line) superexchange interactions.

tuned by either external pressure or by chemical substitution, each of which is able to introduce lattice distortions and to modify the bond lengths and angles [24–29], thus tuning the magnetic order and frustration. For example, in $A_4CoB_2O_{12}$, the chemical pressure (i.e., the substitution of Ba with Sr and/or La, or W with Re) can tune the FM transition temperature [16]. However, the effects of chemical pressure on the magnetic properties of $A_4NiB_2O_{12}$ have not been investigated in detail.

To clarify the above issues, after synthesizing polycrystalline samples of $A_2La_2NiW_2O_{12}$ (A = Sr, Ba), we studied their magnetic properties by means of magnetization, specific heat, neutron scattering, and muon-spin rotation and relaxation (μSR) measurements. The chemical pressure is introduced by substituting Ba with Sr, which suppresses the FM transition temperature from 6.3 to 4.8 K, while the magnetic moments of the Ni^{2+} ions are ferromagnetically aligned along the c axis in both compounds. Our results suggest that the chemical pressure indeed changes the superexchange interactions in $A_2La_2NiW_2O_{12}$, with the B'-O-B-O-B' superexchange path dominating the competition between the FM and AFM interactions. External pressure on $Sr_2La_2NiW_2O_{12}$ or chemical substitution on the Ni site may further tune the magnetic interactions and lead to magnetic frustration.

II. EXPERIMENTAL DETAILS

The $A_2La_2NiW_2O_{12}$ (A = Sr, Ba) polycrystalline samples were prepared by the solid-state reaction method. Stoichiometric amounts of La_2O_3, $BaCO_3$, $SrCO_3$, NiO, and WO_3 powders were used to prepare the materials. The La_2O_3 rare-earth oxide was annealed for 15 h in atmosphere to remove moisture. The powders were then mixed, ground, and sintered at 1200 °C for 24 h. After grinding the samples again, the powders were pressed into pellets and sintered at 1200 °C for extra 48 h. The magnetic-susceptibility and heat-capacity measurements were performed on a Quantum Design magnetic property measurement system (MPMS) and physical property measurement system (PPMS), respectively.

Neutron powder diffraction (NPD) measurements were carried out at the Swiss Neutron Source SINQ of the Paul Scherrer Institute in Villigen, Switzerland. The $A_2La_2NiW_2O_{12}$ powder samples were introduced in cylindrical vanadium cans (8 mm in diameter and 50 mm high) and mounted on a helium cryostat stick (2–300 K). High-resolution room-temperature NPD patterns were recorded at the HRPT powder diffractometer [Ge (822), $\lambda = 1.154$ Å]. To discern the magnetic diffraction peaks, high-intensity NPD patterns were collected at 1.7 K on the DMC diffractome-

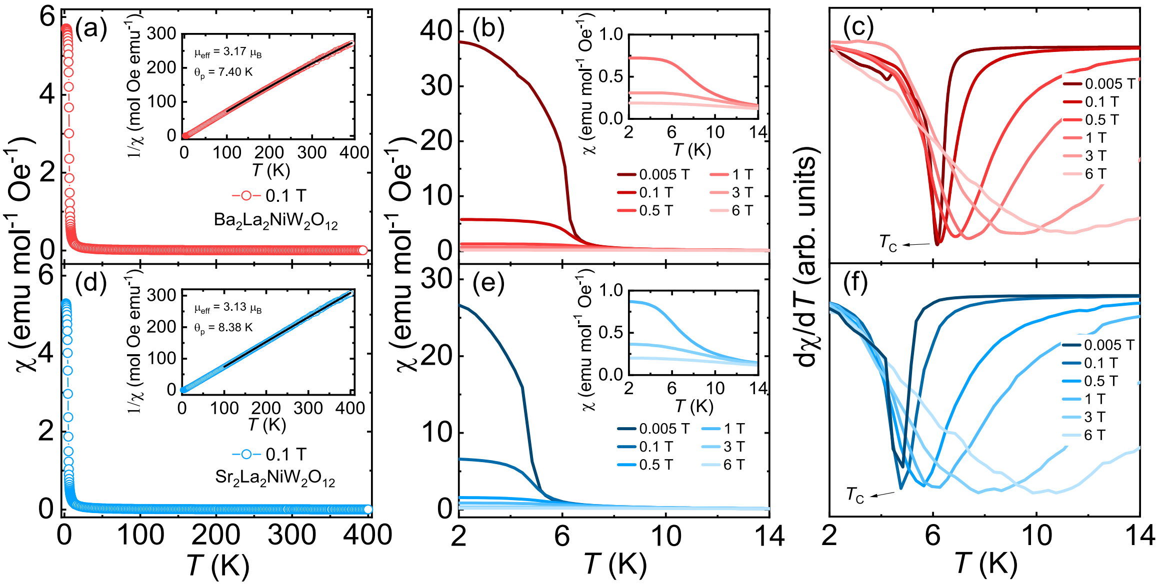

FIG. 2. (a) Temperature-dependent DC magnetic susceptibility $\chi(T)$ of $Ba_2La_2NiW_2O_{12}$ collected in a field of 0.1 T. The inset shows the inverse susceptibility $\chi(T)^{-1}$, with the solid line being a fit to the Curie-Weiss law. (b) Temperature-dependent magnetic susceptibility of $Ba_2La_2NiW_2O_{12}$ measured in various magnetic fields up to 6 T. The inset enlarges the $\chi(T)$ curves collected at $\mu_0 H = 0.5$, 1, and 6 T. Their derivatives with respect to temperature are shown in panel (c). The temperatures where $d\chi/dT$ exhibits a minimum define the Curie temperature T_c and are indicated by an arrow. The analogous results for $Sr_2La_2NiW_2O_{12}$ are shown in the panels (d)–(f), respectively.

ter using a longer wavelength [pyrolitic graphite (002), $\lambda = 2.458$ Å]. The collected NPD patterns were analyzed using the Rietveld package of the FULLPROF suite [30].

The bulk μSR measurements were carried out at the general-purpose surface-muon instrument (GPS) of the Swiss muon source at Paul Scherrer Institut, Villigen, Switzerland. In this study, we performed two types of experiments: zero-field (ZF) and longitudinal-field (LF) μSR measurements. In both cases, we aimed at studying the temperature evolution of the magnetically ordered phase and the spin fluctuations. The μSR spectra were collected upon sample heating and then analyzed by the MUSRFIT software package [31].

III. RESULTS AND DISCUSSION

A. Magnetic susceptibility

The $A_2La_2NiW_2O_{12}$ samples were first characterized by magnetic-susceptibility measurements. Figures 2(a) and 2(d) show the temperature-dependent magnetic susceptibility $\chi(T)$ collected in an applied magnetic field of 0.1 T using a zero-field-cooling (ZFC) protocol. $\chi(T)$ shows a sharp increase close to T_c, the temperature where the Ni^{2+} moments give rise to a FM order. The Curie temperatures T_c can be determined from the derivative of susceptibility with respect to temperature $d\chi/dT$ [see Figs. 2(c) and (2(f)] which, in a 0.1-T applied field, provides a T_c of 6.3 and 4.8 K for $Ba_2La_2NiW_2O_{12}$ and $Sr_2La_2NiW_2O_{12}$, respectively. The magnetic susceptibility was also measured under various magnetic fields up to 6 T. As shown in Figs. 2(b) and 2(e), as the magnetic field increases, the transition becomes broader and T_c moves to higher temperatures, both features typical of ferromagnetic materials. The insets in Figs. 2(a) and 2(d) show the Curie-Weiss fits to the inverse susceptibility (solid lines), which yield Weiss temperatures $\theta_p = 7.4$ K for $Ba_2La_2NiW_2O_{12}$ and $\theta_p = 8.4$ K for $Sr_2La_2NiW_2O_{12}$. The positive θ_p values indicate that FM interactions are dominant in both compounds. The estimated effective moments are $\mu_{\text{eff}} = 3.17\mu_B$ and $3.13\mu_B$ for $Ba_2La_2NiW_2O_{12}$ and $Sr_2La_2NiW_2O_{12}$, respectively. Both are close to the theoretical value of spin-only Ni^{2+} ions ($2.83\mu_B$), i.e., assuming a quenching of the orbital moment, typical of octahedral complexes [32], such as the NiO_6 units in Fig. 1(a).

The FM ground state was further confirmed by field-dependent magnetization measurements (see Fig. 3). For $T < T_c$, a small yet clear magnetic hysteresis loop was observed. In both materials, the magnetization starts to saturate for $\mu_0 H > 5$ T. After substituting Ba with Sr, the magnetism becomes softer. The coercive field of $Ba_2La_2NiW_2O_{12}$ is about 67 mT, while, in $Sr_2La_2NiW_2O_{12}$, it decreases to 4 mT. Thus, in $A_2La_2NiW_2O_{12}$, the chemical pressure suppresses both the magnetization and the T_c, suggesting an enhancement of the magnetic competition. Nevertheless, the FM interactions remain dominant also in $Sr_2La_2NiW_2O_{12}$.

B. Heat capacity

We measured the zero-field heat-capacity of $A_2La_2NiW_2O_{12}$ from 2 to 300 K. The low-T heat-capacity data were also collected under various external fields, up to 9 T. As shown in Fig. 4, in both compounds, there is a sharp λ-like transition at low temperatures, typical of long-range magnetic order. The $C(T)$ data show a distinct peak at $T_c = 6.1$ and 4.7 K for $Ba_2La_2NiW_2O_{12}$ and $Sr_2La_2NiW_2O_{12}$, consistent with the T_c values determined from magnetization data (see Fig. 2). To extract the magnetic contribution, the normal-state (i.e., $T \gg T_c$) specific-heat data were fitted to $C/T = \gamma + \beta T^2$, where $\gamma \equiv 0$, due to the insulating nature of both compounds [see solid lines in Figs. 4(a) and 4(d)]. The derived β values are 0.0013 and 0.0012 J mol^{-1} K^{-4} for $Ba_2La_2NiW_2O_{12}$ and $Sr_2La_2NiW_2O_{12}$, which yield Debye temperatures $\theta_D = 142$ and 145 K, respectively. After subtracting the phonon contribution (i.e., the βT^2 term), the magnetic specific heat C_m/T vs temperature is plotted in Figs. 4(b) and 4(e) for $Ba_2La_2NiW_2O_{12}$ and $Sr_2La_2NiW_2O_{12}$, respectively. Upon increasing the magnetic field, the peak at T_c becomes broader and moves to higher temperatures, once more confirming the FM nature of the magnetic transition in both materials. The zero-field magnetic entropy $S_m(T)$ obtained by integrating $C_m(T)/T$ is shown in Figs. 4(c) and 4(f) for $Ba_2La_2NiW_2O_{12}$ and $Sr_2La_2NiW_2O_{12}$, respectively. In both compounds, at temperatures close to T_c, S_m reaches $R\ln(2)$ (corresponding to $S = 1/2$). In $Ba_2La_2NiW_2O_{12}$, at temperatures above

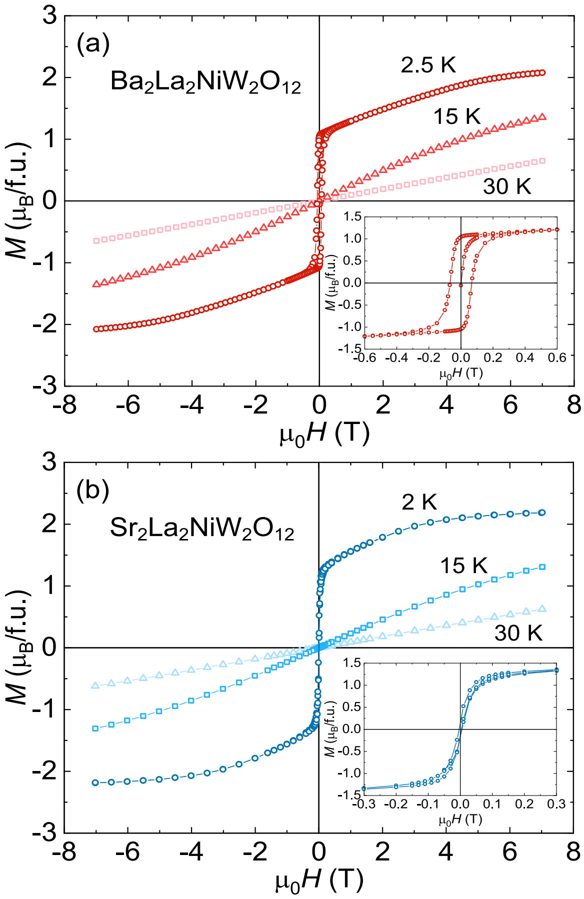

FIG. 3. Field-dependent magnetization $M(H)$ in both the ferromagnetic and paramagnetic states of $Ba_2La_2NiW_2O_{12}$ (a) and $Sr_2La_2NiW_2O_{12}$ (b). Insets highlight the low-field region of $M(H)$ for $Ba_2La_2NiW_2O_{12}$ (at 2.5 K) and $Sr_2La_2NiW_2O_{12}$ (at 2 K), clearly showing the hysteresis loops.

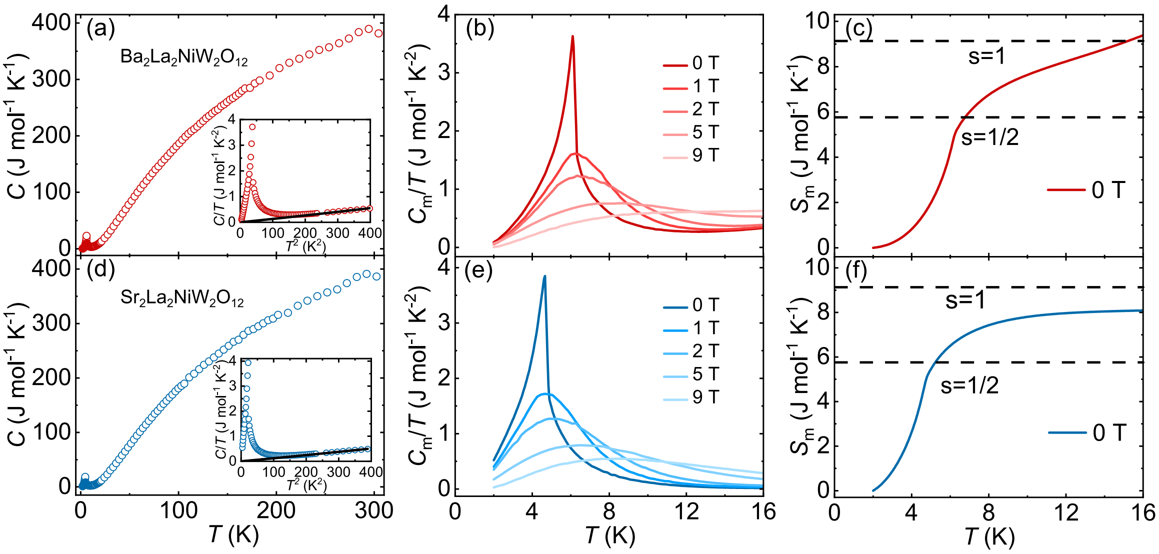

FIG. 4. (a) Temperature-dependent heat capacity of Ba$_2$La$_2$NiW$_2$O$_{12}$ measured in zero-field condition from 2 to 300 K. The inset shows the specific heat C/T vs T^2 below 20 K. The solid line is a fit to $C/T = \gamma + \beta T^2$ in the paramagnetic state, with $\gamma \equiv 0$ reflecting the compound's insulating nature. (b) Temperature dependence of the magnetic contribution to the specific heat C_m/T of Ba$_2$La$_2$NiW$_2$O$_{12}$ in various magnetic fields up to 9 T. (c) The zero-field magnetic entropy $S_m(T)$ obtained from the integration of $C_m(T)/T$ of Ba$_2$La$_2$NiW$_2$O$_{12}$. The dashed lines mark the entropy values $R\ln(2S+1)$, with $S = 1/2$ and 1, respectively. The analogous results for Sr$_2$La$_2$NiW$_2$O$_{12}$ are shown in panels (d)–(f), respectively.

T_c, S_m reaches $R\ln(3)$ (corresponding to $S = 1$), while in Sr$_2$La$_2$NiW$_2$O$_{12}$, S_m is slightly smaller than $R\ln(3)$. Such a deviation is most likely due to an oversubtraction of the phonon contribution from the specific-heat data. To properly subtract the phonon contribution and estimate the magnetic entropy, heat-capacity measurements on the nonmagnetic counterparts, e.g., A_2La$_2$ZnW$_2$O$_{12}$, are highly desirable.

C. Neutron diffraction

To determine the crystal- and magnetic structures of A_2La$_2$NiW$_2$O$_{12}$, neutron powder diffraction patterns were collected at both the paramagnetic (300 K) and ferromagnetic states (1.7 K). The room-temperature patterns were first analyzed by using the space group $R\bar{3}m$ (No. 166), as reported in previous studies [16]. With this model, the powder x-ray diffraction (XRD) patterns could be fitted reasonably well with a goodness of fit $\chi_r^2 \sim 7$. However, in the case of the NPD patterns, although the Bragg peaks were located at the right positions, the $R\bar{3}m$ space group yielded a fairly large $\chi_r^2 \sim 18$, as evinced also from the clear discrepancy between the observed and calculated intensities. This indicates that the space group $R\bar{3}m$ does not describe the crystal structure of A_2La$_2$NiW$_2$O$_{12}$ compounds accurately and, thus, further corrections to the structural model are required. Considering that neutron diffraction is more sensitive to the oxygen atoms than x-ray diffraction [33], the oxygen positions are most likely to require corrections. We found that the space group $R\bar{3}$ (No. 148) reproduces the NPD patterns quite well. In fact, both $R\bar{3}m$ and $R\bar{3}$ space groups belong to the trigonal system, with the latter exhibiting slightly different oxygen positions. Figures 5(a) and 5(b) show the Rietveld refinements of NPD at 300 K using the $R\bar{3}$ space group for both compounds. These refinements yield a significantly reduced $\chi_r^2 \sim 2$, thus confirming that, in both cases, the $R\bar{3}$ space group is more appropriate than $R\bar{3}m$. With $R\bar{3}$, the NiO$_6$ and WO$_6$ octahedra rotate in opposite directions around the c axis, which breaks the mirror symmetry. A similar symmetry breaking has been observed also in the Ba$_2$La$_2$NiTe$_2$O$_{12}$ compound [17]. The refined lattice parameters, atomic positions, and bond lengths/angles, together with the goodnesses of fit, are summarized in Table I for A_2La$_2$NiW$_2$O$_{12}$ compounds.

To clarify the magnetic structure of Ba$_2$La$_2$NiW$_2$O$_{12}$ and Sr$_2$La$_2$NiW$_2$O$_{12}$, the NPD patterns were also collected in the magnetically ordered state (i.e., 1.7 K) using long wavelength neutrons ($\lambda = 2.458$ Å). The LeBail fits of the magnetic diffraction patterns reveal a commensurate magnetic structure with a propagation vector $\boldsymbol{k} = (0, 0, 0)$ for A_2La$_2$NiW$_2$O$_{12}$ compounds. For such a magnetic vector, the little group G_k is identical to the space group $R\bar{3}$, and it includes the symmetry elements $1, 3^+, 3^-, \bar{1}, \bar{3}^+$, and $\bar{3}^-$ [34]. The magnetic unit cell of A_2La$_2$NiW$_2$O$_{12}$ possesses a single orbit with only one site located at the Ni (0, 0, 0) position. For $\boldsymbol{k} = (0, 0, 0)$, G_k has six different irreducible representations (irreps), $\tau 1$, $\tau 2$, $\tau 3$, $\tau 4$, $\tau 5$, and $\tau 6$, among which only $\tau 1$, $\tau 3$, and $\tau 5$ allow for a long-range magnetic order at the Ni site. Table II summarizes the basis vectors of $\tau 1$, $\tau 3$, and $\tau 5$ irreps calculated with BASIREPS. For the $R\bar{3}$ space group, the Ni atoms are located at the 3a site (0, 0, 0), invariant under all the symmetry operations. As a consequence, all the allowed irreps generate a FM coupling with the spins aligned along the c axis for $\tau 1$, or lying within the ab plane for $\tau 3$ and $\tau 5$ (see details in Table II). According to the Rietveld refinements of the 1.7-K NPD pattern [see Figs. 5(c) and 5(d)], the best fits were obtained by using the $\tau 1$ irrep, yielding the smallest $\chi_r^2 = 1.93$ and 2.77 for Ba$_2$La$_2$NiW$_2$O$_{12}$ and Sr$_2$La$_2$NiW$_2$O$_{12}$, respectively. The refined magnetic structure is shown in Fig. 1(b).

TABLE I. Room-temperature lattice parameters, atomic positions, bond lengths and angles, and goodness of fits for $A_2La_2NiW_2O_{12}$ (A = Ba/Sr).

Space group				$R\bar{3}$
Z				19
a (Å)				5.66126(9)/5.59654(5)
c (Å)				27.35363(3)/26.58389(1)
$R_p = 5.53/5.90\%$, $R_{wp} = 7.13/6.42\%$, $\chi_r^2 = 2.53/1.97$				
Atom	Wyckoff	x	y	z
Ba/Sr	6c	0	0	0.1329(7)/0.1340(2)
La	6c	0	0	0.2931(1)/0.2913(2)
Ni	3a	0	0	0
W	6c	0	0	0.4182(5)/0.4215(4)
O1	18f	0.4647(5)/0.4445(1)	0.4715(8)/0.4472(9)	0.1180(3)/0.1216(1)
O2	18f	0.4316(1)/0.4312(6)	0.4537(9)/0.4508(6)	0.2947(2)/0.2926(2)
Bond length: Ni-O2: 2.064(4) Å/2.051(2) Å			Bond length: W-O2: 2.009(6) Å/2.004(2) Å	
Bond angle: ∠Ni-O2-O2: 121.50(5)°/120.62(4)°			Bond angle: ∠O2-W-O2: 84.51(3)°/84.53(2)°	

The magnetic moments of Ni atoms obtained from the refinements are $1.94(2)\mu_B$ and $1.84(3)\mu_B$ for $Ba_2La_2NiW_2O_{12}$ and $Sr_2La_2NiW_2O_{12}$, consistent with their saturation magnetization (see Fig. 3).

D. ZF- and LF-μSR

The large gyromagnetic ratio of muons, combined with their availability as 100% spin-polarized beams, makes ZF-μSR a very sensitive probe for investigating magnetic materials. Here, to study the magnetic properties of $A_2La_2NiW_2O_{12}$ at a local level, we collected a series of ZF-μSR spectra at temperatures covering both the paramagnetic- and ferromagnetic states. Since neutron diffraction data suggest FM ground states for both $Ba_2La_2NiW_2O_{12}$ and $Sr_2La_2NiW_2O_{12}$ (with the Ni^{2+} moments aligned along the c axis), for our μSR measurements we focused on $Ba_2La_2NiW_2O_{12}$ due to its slightly higher T_c value. In a magnetic material with a long-range order, the time evolution of ZF-μSR asymmetry, $A_{ZF}(t)$, encodes both the intrinsic magnetic fields and their distribution at the muon-stopping site [35]. The ZF-μSR spectra of $Ba_2La_2NiW_2O_{12}$ collected at different temperatures are shown in Fig. 6(a). In the paramagnetic state ($T > T_c$), the ZF-μSR spectra exhibit a relatively slow muon-spin depolarization (~0.5–1 μs^{-1} at 10 K), indicating rather weak spin fluctuations. Considering the two muon-stopping sites in $Ba_2La_2NiW_2O_{12}$, attributed to two distinct oxygen sites (see Table I), the ZF-μSR spectra in the paramagnetic state were analyzed using the following model:

$$A_{ZF}(t) = \sum_{i=1}^{2} A_i e^{-\lambda_i^L t}. \quad (1)$$

TABLE II. Basis vectors of irreps $\tau 1$, $\tau 3$, and $\tau 5$, as calculated by BASIREPS.

Site	$\tau 1$	$\tau 3$	$\tau 5$
Ni	(0, 0, 1)	(1, 0, 0)	(1, 0, 0)
	(0, 0, 0)	(−0.58, −1.15, 0)	(0.58, 1.15, 0)

Here, λ_i^L represent the longitudinal muon-spin relaxation rates, while A_i are the asymmetries of the two nonequivalent muon-stopping sites.

In the FM state ($T < T_c$), the ZF-μSR spectra are characterized by highly-damped oscillations, typical of long-range magnetic order. These are clearly visible in Fig. 6(b), where short-time oscillations are superimposed on a long-time slow relaxation. The ZF-μSR spectra in the FM state were, hence, analyzed using the following model:

$$A_{ZF}(t) = \sum_{i=1}^{2} A_i\left[\alpha \cos(\omega_i t + \phi) e^{-\lambda_i^T t} + (1 - \alpha) e^{-\lambda_i^L t}\right]. \quad (2)$$

Here, α and $1 - \alpha$ are the oscillating (i.e., transverse) and nonoscillating (i.e., longitudinal) fractions of the μSR signal, respectively, whose initial total asymmetry is equal to A_1 and A_2. In polycrystalline materials with a long-range magnetic order, one expects $\alpha = 2/3$, since statistically one-third of the muon spins are aligned parallel to the local field direction (i.e., $S_\mu \parallel B_{int}$) and, hence, do not precess; ω_i ($= \gamma_\mu B_i^{int}$) represent the muon-spin precession frequencies, with $\gamma_\mu = 2\pi \times 135.5$ MHz/T the muon gyromagnetic ratio and B_i^{int} the local fields sensed by muons; λ_i^T are the transverse muon-spin relaxation rates, reflecting the internal field distributions; ϕ is a shared initial phase.

The derived fitting parameters are summarized in Figs. 6(c)–6(e). B_i^{int}, λ_i^T, and λ_i^L all show a distinct anomaly at T_c. The T_c determined from ZF-μSR is consistent with the value determined from magnetic susceptibility and heat capacity (see Figs. 2 and 4). As shown in Fig. 6(c), below T_c, there are two distinct internal fields, here reflecting the two different muon-stopping sites. In the FM state, the temperature evolution of $B_i^{int}(T)$ resembles the typical mean-field curve. To estimate the zero-temperature internal field, $B_i^{int}(T)$ was analyzed by means of a phenomenological model:

$$B_i^{int}(T) = B_i^{int}(0)\left[1 - \left(\frac{T}{T_c}\right)^{\gamma}\right]^{\delta}, \quad (3)$$

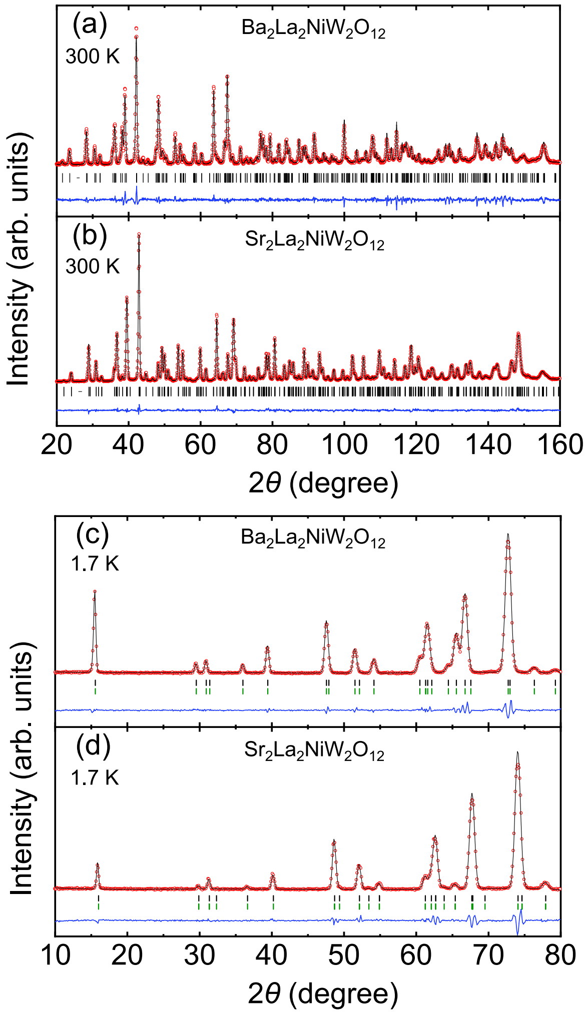

FIG. 5. Rietveld fits of the NPD patterns of $Ba_2La_2NiW_2O_{12}$ collected in the paramagnetic state (300 K) (a) and in the magnetically ordered state (1.7 K) (c). The analogous results for $Sr_2La_2NiW_2O_{12}$ are shown in panels (b) and (d), respectively. Red symbols show the experimental data, while black lines are the refined profiles. Blue lines at the bottom show the residuals, i.e., the difference between the calculated and the experimental data. The black and green ticks under the patterns indicate the positions of nuclear and magnetic reflections, respectively.

where $B_i^{\text{int}}(0)$ is the zero-temperature internal field, while γ and δ represent two empirical parameters. As shown by solid lines in Fig. 6(c), the above model describes the data reasonably well, yielding $B_1^{\text{int}}(0) = 0.30$ T and $B_2^{\text{int}}(0) = 0.10$ T for $Ba_2La_2NiW_2O_{12}$. The standard deviation for B_i^{int} is less than 2 mT. The resulting power exponents are $\gamma = 5.5(2)$ and $\delta = 0.54(2)$ for $B_1^{\text{int}}(T)$, and $\gamma = 4.6(2)$ and $\delta = 0.26(1)$ for $B_2^{\text{int}}(T)$. The lack of any anomalies in $B_i^{\text{int}}(T)$ below T_c is consistent with the simple FM structure of $Ba_2La_2NiW_2O_{12}$ (see Fig. 1). In fact, in some complex magnetic materials with multiple transitions, one observes a more complex $B^{\text{int}}(T)$, since changes in magnetic structure are reflected in the local-field distribution [36].

The transverse muon-spin relaxation rate λ^{T} reflects the static magnetic field distribution at the muon-stopping site and is also affected by dynamical effects such as spin fluctuations, while its longitudinal counterpart λ^{L} is solely determined by spin fluctuations. The $\lambda_i^{\text{T}}(T)$ of $Ba_2La_2NiW_2O_{12}$ exhibits a behavior typical of magnetic materials with a long-range order [36,37], i.e., diverging at T_c and continuously decreasing well inside the magnetic state [see Fig. 6(d)]. In the paramagnetic state, λ_i^{T} is zero, due to the lack of a magnetic moment in the absence of an external field. The $\lambda_i^{\text{L}}(T)$ in Fig. 6(e) shows a behavior similar to that of $\lambda_i^{\text{T}}(T)$, i.e., $\lambda_i^{\text{L}}(T)$ diverges near T_c, followed by a significant drop at $T < T_c$, indicating that spin fluctuations are the strongest close to the onset of the FM order. Note that the absolute values of longitudinal relaxation are much smaller than the transverse ones. Thus, at 1.5 K, $\lambda^{\text{L}}/\lambda^{\text{T}} \sim 0.097$ and 0.002 for the two different muon-stopping sites. In the paramagnetic state (i.e., $T > 8$ K), λ_i^{L} is also very small, suggesting weak spin fluctuations in both the ferromagnetic and paramagnetic states of $Ba_2La_2NiW_2O_{12}$. Such weak spin fluctuations are further supported by LF-μSR measurements. Figure 7 shows the 2-K LF-μSR spectra collected in longitudinal fields of 0.1 and 0.5 T. Once the external field exceeds the internal field (here, ~0.3 T), the μSR spectra become almost flat. This suggests that, in $Ba_2La_2NiW_2O_{12}$, muon spins are fully decoupled from the electronic magnetic moments in a field of 0.5 T.

IV. DISCUSSION

Although our comprehensive set of measurements suggests that both $Ba_2La_2NiW_2O_{12}$ and $Sr_2La_2NiW_2O_{12}$ have FM ground states, the magnetic susceptibility and neutron diffraction results indicate that the competition between FM and AFM couplings is indeed tuned by the chemical pressure induced by the substitution of Ba- with the smaller Sr ions. To understand this, we examine the crystal-structure parameters of $A_2La_2NiW_2O_{12}$ (see details in Table I), including the bond lengths and angles. The latter are directly related to the magnetic superexchange interactions and, thus, control the magnetic properties. In $A_4B'B_2O_{12}$, the $B'O_6$ octahedra share their corners with the BO_6 octahedra via oxygen atoms, thus leading to two superexchange interaction paths, i.e., B'-O-B-O-B' and B'-O-O-B' [see details in Fig. 1(c)]. According to the Goodenough-Kanamori rule, which provides the signs of the competitive interactions that are responsible for non-collinear spin ordering [38–40], the B'-O-B-O-B' superexchange interaction (with $\angle$O-B-O $\sim 90^\circ$) favors a FM coupling, while the B'-O-O-B' path (with $\angle B'$-O-O $\sim 120^\circ$–180°) allows for an AFM coupling. Although the $R\bar{3}$ space group implies reduced O-B-O and B'-O-O bond angles with respect to the previously reported $R\bar{3}m$ space group [16], the change is such that the FM or AFM character of the superexchange interactions is maintained. For instance, in $Ba_2La_2NiW_2O_{12}$, $R\bar{3}m$ gives $\angle$Ni-O2-O2 $= 137.2^\circ$ and $\angle$O2-W-O2 $= 86.7^\circ$, while in $R\bar{3}$ these bond angles become 121.5° and 84.5°. Consequently, the B'-O-B-O-B' and B'-O-O-B' superexchange interaction paths remain valid also in the $R\bar{3}$ space group.

The competition between these FM and AFM interactions eventually determines the magnetic ground state of $A_4B'B_2O_{12}$. Since Sr has a smaller atomic radius than Ba, by replacing Ba with Sr the lattice constants along the a and c axes are reduced by 1.14% and 2.81%, respectively, the

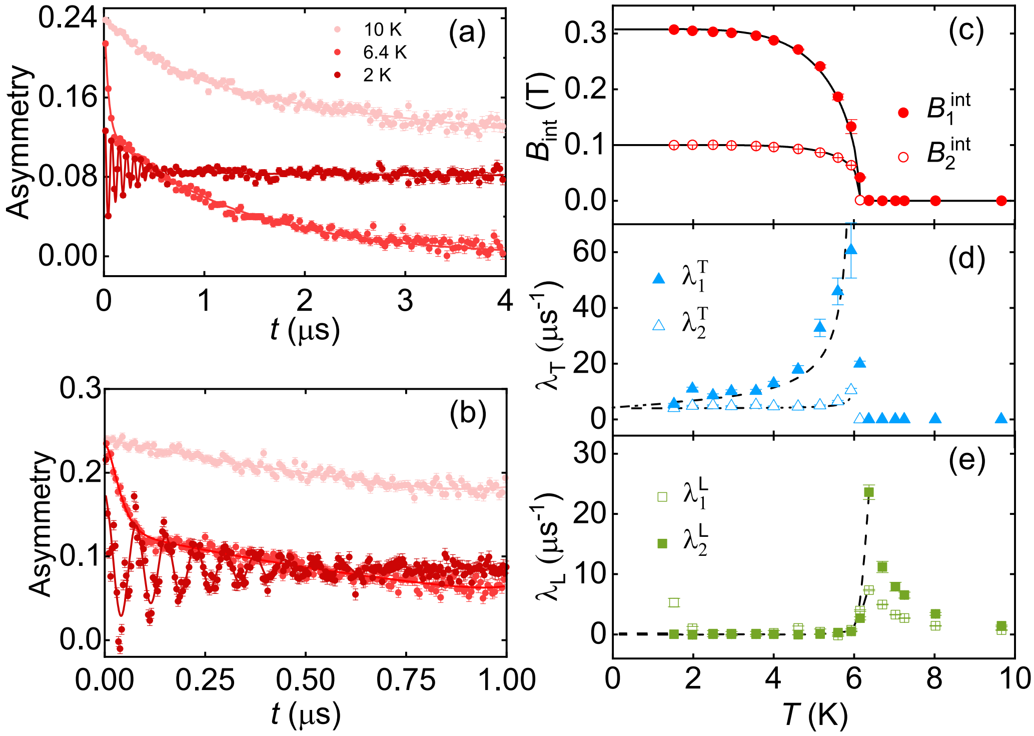

FIG. 6. (a) Representative zero-field μSR spectra of $Ba_2La_2NiW_2O_{12}$, collected at various temperatures covering both the paramagnetic and ferromagnetic states. The short-time spectra, illustrating the coherent oscillations caused by the long-range FM order, are displayed in panel (b). Solid lines through the data are fits to Eqs. (1) and (2) (see text for details). Temperature dependence of the internal field $B_i^{\mathrm{int}}(T)$ (c), transverse muon-spin relaxation rate (also known as damping rate) λ_i^{T} (d), and longitudinal muon-spin relaxation rate λ_i^{L} (e) for $Ba_2La_2NiW_2O_{12}$, as derived from the ZF-μSR data analysis. Solid lines in (c) are fits to Eq. (3); dashed lines in (d) and (e) are guides to the eyes. For clarity reasons, in panel (e), λ_1^{L} was multiplied by a factor 10.

Ni-O bond length decreases from 2.064 to 2.051 Å, while the Ni-O2-O2 bond angle increases from 121.50° to 120.62°. By contrast, the W-O bond length and the O2-W-O2 bond angle are less affected, most likely because the W-O2 layer is further away from the Ba or Sr layers [see Fig. 1(a)]. The O2-W-O2 bond angle increases slightly from 84.51° to 84.53°. The changes of Ni-O2-O2 and O2-W-O2 bond angles induced by chemical pressure (i.e., the substitution of Ba by Sr) tune the competition between FM- and AFM superexchange interactions in $A_2La_2NiW_2O_{12}$. The physical pressure might further tune the competition between the FM and AFM interactions, thus yielding magnetic frustration. Previous studies reveal that the magnetic ground state of $A_4B'B_2O_{12}$ can also be tuned by chemical substitution on the B sites [16]. The substitution of Ni on the B' site may enhance the B'-O-O-B' AFM interactions and stabilize the AFM ground state. For instance, $Ba_2La_2MnW_2O_{12}$ shows an AFM order below 1.7 K [16]. The Ni^{2+} ions can also be substituted by Cu^{2+} ions, but such case has not yet been studied, although it may represent another interesting compound to exhibit magnetic frustration. Finally, the introduction of magnetic ions on the A site (e.g., the substitution of Ba^{2+} or Sr^{2+} with Eu^{2+}), whose magnetic interactions can compete with the above superexchange interactions, may lead to exotic magnetic properties.

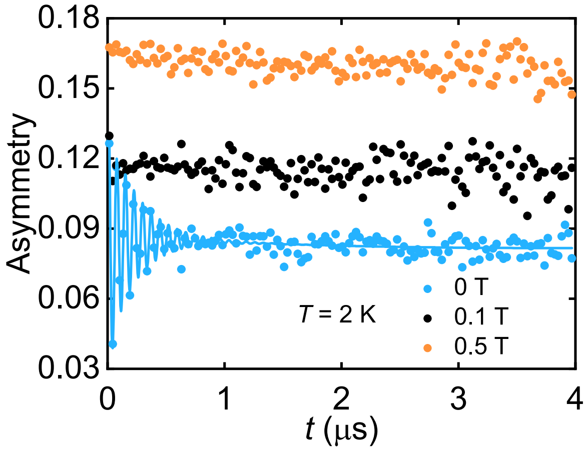

FIG. 7. LF-μSR spectra of $Ba_2La_2NiW_2O_{12}$ collected at 2 K in magnetic fields of 0, 0.1, and 0.5 T. Here, we use a longitudinal muon-spin configuration, i.e., $p_\mu \parallel S_\mu$, with the applied field being parallel to the muon-spin direction. Muon spins are fully decoupled once the external field overcomes the internal field.

V. CONCLUSION

To summarize, we studied the effects of chemical pressure on the magnetic triangular-lattice compounds $A_2La_2NiW_2O_{12}$ (A = Sr, Ba). Their magnetic properties (due to the Ni^{2+} ions) were investigated by means of magnetic susceptibility, specific heat, neutron diffraction, and μSR spectroscopy. When replacing Ba with Sr, chemical pressure is introduced which can tune the competition between the FM and AFM superexchange interactions. While the Curie temperature T_c is suppressed from 6.3 to 4.8 K, the FM interactions still persist in $Sr_2La_2NiW_2O_{12}$. According to the refinements of neutron diffraction patterns, in both compounds the magnetic moments of Ni atoms are aligned along the c axis, with a propagation vector $\boldsymbol{k} = (0, 0, 0)$. By using ZF-$\mu$SR measurements, we could follow the temperature evolution of the spin fluctuations and of the local magnetic fields. The estimated internal fields at zero temperature for the two different muon-stopping sites are 0.31 and 0.1 T. The smooth transverse muon-spin relaxation rates λ_T in the ordered phase confirm the simple FM structure of $A_2La_2NiW_2O_{12}$. In both materials, spin fluctuations are rather weak, reflected in a small longitudinal muon-spin relaxation rate in both the ferromagnetic and paramagnetic states. In the future, it could be interesting to check if the combined physical pressure and chemical substitution on the A and B' sites can further tune the magnetic competitions in $Sr_2La_2NiW_2O_{12}$, and eventually lead to magnetic frustration or to a quantum spin-liquid state.

ACKNOWLEDGMENTS

This work was supported by the Natural Science Foundation of Shanghai (Grants No. 21ZR1420500 and No. 21JC1402300), the Natural Science Foundation of Chongqing (Grant No. 2022NSCQ-MSX1468), and the Schweizerische Nationalfonds zur Förderung der Wissenschaftlichen Forschung (SNF) (Grants No. 200021_188706 and No. 206021_139082). Y.X. acknowledges support from the Shanghai Pujiang Program (Grant No. 21PJ1403100) and the Natural Science Foundation of China (Grant No. 12274125).

[1] K. Binder and A. P. Young, Spin glasses: Experimental facts, theoretical concepts, and open questions, Rev. Mod. Phys. **58**, 801 (1986).

[2] M. F. Collins and O. A. Petrenko, Triangular antiferromagnets, Can. J. Phys. **75**, 605 (1997).

[3] R. Moessner and A. P. Ramirez, Geometrical frustration, Phys. Today **59**(2), 24 (2006).

[4] L. Balents, Spin liquids in frustrated magnets, Nature (London) **464**, 199 (2010).

[5] Z. Ma, J. Wang, Z.-Y. Dong, J. Zhang, S. Li, S.-H. Zheng, Y. Yu, W. Wang, L. Che, K. Ran, S. Bao, Z. Cai, P. Čermák, A. Schneidewind, S. Yano, J. S. Gardner, X. Lu, S.-L. Yu, J.-M. Liu, S. Li *et al.*, Spin-Glass Ground State in a Triangular-Lattice Compound $YbZnGaO_4$, Phys. Rev. Lett. **120**, 087201 (2018).

[6] A. P. Ramirez, A. Hayashi, R. J. Cava, R. Siddharthan, and B. S. Shastry, Zero-point entropy in 'spin ice', Nature (London) **399**, 333 (1999).

[7] J. Khatua, M. Gomilšek, J. C. Orain, A. M. Strydom, Z. Jagličić, C. V. Colin, S. Petit, A. Ozarowski, L. Mangin-Thro, K. Sethupathi, M. S. R. Rao, A. Zorko, and P. Khuntia, Signature of a randomness-driven spin-liquid state in a frustrated magnet, Commun. Phys. **5**, 99 (2022).

[8] Y. Shen, Y.-D. Li, H. C. Walker, P. Steffens, M. Boehm, X. Zhang, S. Shen, H. Wo, G. Chen, and J. Zhao, Fractionalized excitations in the partially magnetized spin liquid candidate $YbMgGaO_4$, Nat. Commun. **9**, 4138 (2018).

[9] A. P. Ramirez, Strongly geometrically frustrated magnets, Annu. Rev. Mater. Sci. **24**, 453 (1994).

[10] J. E. Greedan, Geometrically frustrated magnetic materials, J. Mater. Chem. **11**, 37 (2001).

[11] H. Kawamura, Universality of phase transitions of frustrated antiferromagnets, J. Phys.: Condens. Matter **10**, 4707 (1998).

[12] J. Jaklič and P. Prelovšek, Finite-temperature properties of doped antiferromagnets, Adv. Phys. **49**, 1 (2000).

[13] G. H. Wannier, Antiferromagnetism. The triangular Ising net, Phys. Rev. **79**, 357 (1950).

[14] H. Y. Lv, W. J. Lu, D. F. Shao, Y. Liu, and Y. P. Sun, Strain-controlled switch between ferromagnetism and antiferromagnetism in $1T$-CrX_2 (X = Se, Te) monolayers, Phys. Rev. B **92**, 214419 (2015).

[15] J. M. Longo, L. Katz, and R. Ward, Rhenium-containing complex metal oxides of the formula type $A_4Re_2MO_{12}$, Inorg. Chem. **4**, 235 (1965).

[16] R. Rawl, M. Lee, E. S. Choi, G. Li, K. W. Chen, R. Baumbach, C. R. dela Cruz, J. Ma, and H. D. Zhou, Magnetic properties of the triangular lattice magnets $A_4B'B_2O_{12}$ (A = Ba, Sr, La; B' = Co, Ni, Mn; B = W, Re), Phys. Rev. B **95**, 174438 (2017).

[17] M. Saito, M. Watanabe, N. Kurita, A. Matsuo, K. Kindo, M. Avdeev, H. O. Jeschke, and H. Tanaka, Successive phase transitions and magnetization plateau in the spin-1 triangular-lattice antiferromagnet $Ba_2La_2NiTe_2O_{12}$ with small easy-axis anisotropy, Phys. Rev. B **100**, 064417 (2019).

[18] Y. Kojima, M. Watanabe, N. Kurita, H. Tanaka, A. Matsuo, K. Kindo, and M. Avdeev, Quantum magnetic properties of the spin-$\frac{1}{2}$ triangular-lattice antiferromagnet $Ba_2La_2CoTe_2O_{12}$, Phys. Rev. B **98**, 174406 (2018).

[19] Y. Doi, M. Wakeshima, K. Tezuka, Y. J. Shan, K. Ohoyama, S. Lee, S. Torii, T. Kamiyama, and Y. Hinatsu, Crystal structures, magnetic properties, and DFT calculation of B-site defected 12L-perovskites $Ba_2La_2MW_2O_{12}$ (M = Mn, Co, Ni, Zn), J. Phys.: Condens. Matter **29**, 365802 (2017).

[20] M. Lee, J. Hwang, E. S. Choi, J. Ma, C. R. Dela Cruz, M. Zhu, X. Ke, Z. L. Dun, and H. D. Zhou, Series of phase transitions and multiferroicity in the quasi-two-dimensional spin-$\frac{1}{2}$ triangular-lattice antiferromagnet $Ba_3CoNb_2O_9$, Phys. Rev. B **89**, 104420 (2014).

[21] K. Yokota, N. Kurita, and H. Tanaka, Magnetic phase diagram of the $S = \frac{1}{2}$ triangular-lattice Heisenberg antiferromagnet $Ba_3CoNb_2O_9$, Phys. Rev. B **90**, 014403 (2014).

[22] J. Hwang, E. S. Choi, F. Ye, C. R. Dela Cruz, Y. Xin, H. D. Zhou, and P. Schlottmann, Successive Magnetic Phase Transitions and Multiferroicity in the Spin-one Triangular-Lattice Antiferromagnet $Ba_3NiNb_2O_9$, Phys. Rev. Lett. **109**, 257205 (2012).

[23] M. Lee, E. S. Choi, X. Huang, J. Ma, C. R. Dela Cruz, M. Matsuda, W. Tian, Z. L. Dun, S. Dong, and H. D. Zhou, Magnetic phase diagram and multiferroicity of $Ba_3MnNb_2O_9$: A spin-$\frac{5}{2}$ triangular lattice antiferromagnet with weak easy-axis anisotropy, Phys. Rev. B **90**, 224402 (2014).

[24] A. Möller, N. E. Amuneke, P. Daniel, B. Lorenz, C. R. dela Cruz, M. Gooch, and P. C. W. Chu, $A\text{Ag}_2M[\text{VO}_4]_2$ (A = Ba, Sr; M = Co, Ni): A series of ferromagnetic insulators, Phys. Rev. B **85**, 214422 (2012).

[25] A. A. Tsirlin, A. Möller, B. Lorenz, Y. Skourski, and H. Rosner, Superposition of ferromagnetic and antiferromagnetic spin chains in the quantum magnet $\text{BaAg}_2\text{Cu}[\text{VO}_4]_2$, Phys. Rev. B **85**, 014401 (2012).

[26] Y. Sun, Z. Liu, W. Zhang, X. Chu, Y. Cong, K. Huang, and S. Feng, Unfolding B–O–B bonds for an enhanced ORR performance in ABO_3-type perovskites, Small **15**, 1803513 (2019).

[27] K. Sengupta, M. K. Forthaus, H. Kubo, K. Katoh, K. Umeo, T. Takabatake, and M. M. Abd-Elmeguid, Geometrical frustration versus magnetic order in the heavy-fermion antiferromagnet YbAgGe under high pressure, Phys. Rev. B **81**, 125129 (2010).

[28] Y. Jiao, Y.-W. Fang, J. Sun, P. Shan, Z. Yu, H. L. Feng, B. Wang, H. Ma, Y. Uwatoko, K. Yamaura, Y. Guo, H. Chen, and J. Cheng, Coupled magnetic and structural phase transitions in the antiferromagnetic polar metal $\text{Pb}_2\text{CoOsO}_6$ under pressure, Phys. Rev. B **102**, 144418 (2020).

[29] R. Gebauer, S. Serra, G. L. Chiarotti, S. Scandolo, S. Baroni, and E. Tosatti, Noncolinear spin polarization from frustrated antiferromagnetism: A possible scenario for molecular oxygen at high pressure, Phys. Rev. B **61**, 6145 (2000).

[30] J. Rodríguez-Carvajal, Recent advances in magnetic structure determination by neutron powder diffraction, Phys. B: Condens. Matter **192**, 55 (1993).

[31] A. Suter and B. M. Wojek, Musrfit: A free platform-independent framework for μSR data analysis, Phys. Procedia **30**, 69 (2012).

[32] A. F. Orchard, *Magnetochemistry*, Oxford Chemistry Primers (Oxford University Press, Oxford, 2003)

[33] A. Furrer, *Neutron Scattering in Novel Materials* (World Scientific, Singapore, 2000).

[34] J. Rodríguez-Carvajal, BASIREPS: A program for calculating irreducible representation of little groups and basis functions of polar and axial vector properties, 2010, part of FullProf Suite, ILL, https://www.ill.eu/sites/fullprof/php/programsfa7c.html?pagina=GBasireps.

[35] A. Yaouanc and P. D. de Réotier, *Muon Spin Rotation, Relaxation, and Resonance: Applications to Condensed Matter* (Oxford University Press, Oxford, 2011).

[36] X. Y. Zhu, H. Zhang, D. J. Gawryluk, Z. X. Zhen, B. C. Yu, S. L. Ju, W. Xie, D. M. Jiang, W. J. Cheng, Y. Xu, M. Shi, E. Pomjakushina, Q. F. Zhan, T. Shiroka, and T. Shang, Spin order and fluctuations in the EuAl_4 and EuGa_4 topological antiferromagnets: A μSR study, Phys. Rev. B **105**, 014423 (2022).

[37] L. M. Tran, M. Babij, L. Korosec, T. Shang, Z. Bukowski, and T. Shiroka, Magnetic phase diagram of Ca-substituted EuFe_2As_2, Phys. Rev. B **98**, 104412 (2018).

[38] J. B. Goodenough, Theory of the role of covalence in the perovskite-type manganites $[\text{La}, M(\text{II})]\text{MnO}_3$, Phys. Rev. **100**, 564 (1955).

[39] J. Kanamori, Superexchange interaction and symmetry properties of electron orbitals, J. Phys. Chem. Solids **10**, 87 (1959).

[40] J. M. D. Coey, *Magnetism and Magnetic Materials* (Cambridge University Press, Cambridge, 2010).